





Article

Enhancement of Ni-NiO-CeO₂ Interaction on Ni-CeO₂/Al₂O₃-MgO Catalyst by Ammonia Vapor Diffusion Impregnation for CO₂ Reforming of CH₄

Sabaithip Tungkamani ^{1,2} , Saowaluk Intarasiri ³, Wassachol Sumarasingha ¹ , Tanakorn Ratana ^{1,2}  and Monrudee Phongaksorn ^{1,2,*} 

¹ Department of Industrial Chemistry, Faculty of Applied Science, King Mongkut's University of Technology North Bangkok, Bangkok 10800, Thailand; sabaithip.t@sci.kmutnb.ac.th (S.T.); w.sumarasingha@gmail.com (W.S.); tanakorn.r@sci.kmutnb.ac.th (T.R.)

² Research and Development Center for Chemical Engineering Unit Operation and Catalyst Design (RCC), King Mongkut's University of Technology North Bangkok, Bangkok 10800, Thailand

³ Faculty of Science, Energy and Environment, King Mongkut's University of Technology North Bangkok, Rayong 21120, Thailand; saowaluk.i@sciee.kmutnb.ac.th

* Correspondence: monrudee.p@sci.kmutnb.ac.th

Abstract: Ni-based catalysts have been widely used for the CO₂ reforming of methane (CRM) process, but deactivation is their main problem. This study created an alternative electronic Ni-NiO-CeO₂ interaction on the surface of 5 wt% Ni-5 wt% CeO₂/Al₂O₃-MgO (5Ni5Ce(xh)/MA) catalysts to enhance catalytic potential simultaneously with coke resistance for the CRM process. The Ni-NiO-CeO₂ network was developed on Al₂O₃-MgO through layered double hydroxide synthesis via our ammonia vapor diffusion impregnation method. The physical properties of the fresh catalysts were analyzed employing FESEM, N₂ physisorption, and XRD. The chemical properties on the catalyst surface were analyzed employing H₂-TPR, XPS, H₂-TPD, CO₂-TPD, and O₂-TPD. The CRM performances of reduced catalysts were evaluated at 600 °C under ambient pressure. Carbon deposits on spent catalysts were determined quantitatively and qualitatively by TPO, FESEM, and XRD. Compared to 5 wt% Ni-5 wt% CeO₂/Al₂O₃-MgO prepared by the traditional impregnation method, the electronic interaction of the Ni-NiO-CeO₂ network with the Al₂O₃-MgO support was constructed along the time of ammonia diffusion treatment. The electronic interaction in the Ni-NiO-CeO₂ nanostructure of the treated catalyst develops surface hydroxyl sites with an efficient pathway of OH* and O* transfer that improves catalytic activities and coke oxidation.

Keywords: CO₂ reforming of methane; Ni-CeO₂ catalyst; Ni-NiO-CeO₂ interaction; surface hydroxyl; coke deposition



Citation: Tungkamani, S.; Intarasiri, S.; Sumarasingha, W.; Ratana, T.; Phongaksorn, M. Enhancement of Ni-NiO-CeO₂ Interaction on Ni-CeO₂/Al₂O₃-MgO Catalyst by Ammonia Vapor Diffusion Impregnation for CO₂ Reforming of CH₄. *Molecules* **2024**, *29*, 2803. <https://doi.org/10.3390/molecules29122803>

Academic Editors: Barbara Bonelli, Laura Santamaria and Maria Cortazar

Received: 28 March 2024

Revised: 15 May 2024

Accepted: 8 June 2024

Published: 12 June 2024

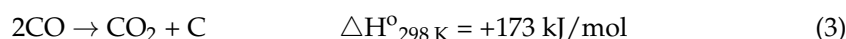
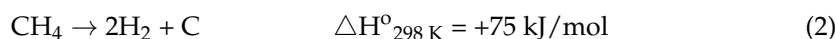


Copyright: © 2024 by the authors. Licensee MDPI, Basel, Switzerland. This article is an open access article distributed under the terms and conditions of the Creative Commons Attribution (CC BY) license (<https://creativecommons.org/licenses/by/4.0/>).

1. Introduction

The unprecedented climate change mainly caused by greenhouse gases is becoming critical. Up to the present day, alternative sources of energy have been generated and developed to decrease greenhouse gas emissions [1,2]. The concentration of greenhouse gases is still at an all-time high. Carbon dioxide reforming of methane (CRM) (Equation (1)) is a significant catalytic process that commercially converts two key greenhouse gases (methane (CH₄) and carbon dioxide (CO₂)) into syngas, a gas mixture composed primarily of hydrogen (H₂) and carbon monoxide (CO) [3–5]. The syngas produced with an approximately equal H₂/CO ratio from the CRM process can be effectively utilized as a precursor for chemical industry production and for green fuel synthesis. In recent decades, Ni-based formulations have been considered as practical CRM catalysts because of their substantial activity with economic cost. However, fast and continuous deactivation is a critical issue for traditional Ni-based catalysts. During the reaction, Ni-based-catalyst-supported metal

oxide can be impeded by metal sintering and coke deposition [6–9]. Over the catalyst surface, metal sintering is caused by a high operating temperature, while coke is formed and grown via side reactions, methane cracking (Equation (2)), and the Boudouard reaction (Equation (3)). Moreover, the side reaction that consumes H_2 and causes the low H_2/CO ratio in the syngas product is the reverse water–gas shift (RWGS, Equation (4)) [10,11].



Several studies revealed how CeO_2 improves the catalyst activity and stability of Ni-based catalysts. When CeO_2 plays a vital role as a support for Ni-based catalysts, Ni sintering and coke deposition can be simultaneously resisted through the Ni- CeO_2 interaction and oxygen storage properties of CeO_2 . Nonetheless, CeO_2 has a low surface area compared to other available supports (Al_2O_3 , $MgO-Al_2O_3$, SBA-15) [12–14]. As a promoter, the addition of CeO_2 to a Ni/ Al_2O_3 catalyst forms $Ce_{1-x}Ni_xO_2$ and $CeAlO_3$ phases on the catalyst surface. Thus, the oxygen transfer and reducibility of the promoted catalyst can be improved to raise its catalytic activity and carbon resistance [15–18].

Our group has developed a novel ammonia vapor diffusion impregnation method that allows the size of the hierarchical nanostructures of the modified catalyst surface to be controlled by the ammonia vapor diffusion time. Previously, the hierarchical structure and basicity of the layered nanosheets on 10 wt% Ni/ $MgO-Al_2O_3$ prepared by ammonia vapor diffusion impregnation for 20 h exhibited that the hierarchical nanostructures on the surface can enhance CO_2 adsorption–dissociation and prevent coke formation for the CRM process [19]. A 10 wt% Ni-1 wt% ZrO_2/Al_2O_3 catalyst prepared by a similar method with an ammonia diffusion time of 6 h demonstrated an improvement in the steam activation–dissociation and coke resistance for the combined steam and CO_2 reforming of methane (CSCRM) process operated under low-temperature and low-steam conditions. This can be attributed to the very dispersive nanosheets and redox properties of the ZrO_2 promoter that produces the number of the OH^* and O^* species on the surface [20]. Consequently, it would be interesting to develop the heterogeneity of Ni- CeO_2 networks on catalyst surface through time-controlled ammonia diffusion treatment to investigate its effect on properties, CRM performance, and deactivation.

Herein, this present work prepared a 5 wt% Ni-5 wt% CeO_2 -supported $MgO-Al_2O_3$ catalyst by the ammonia vapor diffusion impregnation method (5Ni5Ce(xh)/MA). During the preparation, a nickel–cerium network nanostructure was initiated and grown during the ammonia diffusion treatment. Accordingly, two treatment times (6 h and 12 h) were applied to study the electronic effects of size and different network nanostructure morphologies on the catalyst surface. Thus, the physical properties were obtained via field emission scanning electron microscopy (FESEM), N_2 physisorption analysis, and X-ray diffraction (XRD) analysis. The chemical insights into the surface interactions of the nanostructure on 5Ni5Ce(xh)/MA were evaluated by employing X-ray photoelectron spectroscopy (XPS), temperature-programmed reduction in H_2 (H_2 -TPR), temperature-programmed desorption of H_2 (H_2 -TPD), temperature-programmed desorption of O_2 (O_2 -TPD), and temperature-programmed desorption of CO_2 (CO_2 -TPD). The CRM catalytic performance was demonstrated in a tubular reactor at 600 °C for 16 h under atmospheric pressure. After the reaction, the carbon deposition was assessed using temperature-programmed oxidation (TPO), FESEM, and XRD. The above-mentioned effects on catalytic characteristics were elaborated and compared to the 5 wt% Ni-5 wt% CeO_2 -supported $MgO-Al_2O_3$ prepared by the traditional impregnation method (5Ni5Ce/MA).

2. Results and Discussion

2.1. Physical Properties

The surface morphologies of the calcined catalysts were investigated by means of FE-SEM images (Figure 1a–c) which show the changes in surface structure caused by ammonia vapor treatment. Compared to the morphology of 5Ni5Ce/MA (Figure 1a), the network of the metal oxide nanoparticles is generated over the surface of 5Ni5Ce(6 h)/MA (Figure 1b). This network of metal oxide nanoparticles is clearly visible on 5Ni5Ce(20 h)/MA (Figure 1c), implying the growth of the NiO-CeO₂ interaction throughout the ammonia vapor diffusion. This can be explained by layered double hydroxide (LDH) synthesis via ammonia vapor diffusion impregnation [19–21]. When ammonia vapor is dissolved into the impregnated nickel–cerium nitrate solution on the support, a limited amount of hydroxide ions are produced, conducting the slow growth of the layered double hydroxide $[\text{Ni}_{1-x}\text{Ce}_x(\text{OH})_2]^{2+}(\text{NO}_3)_z \cdot n\text{H}_2\text{O}$ throughout the diffusion time [22–24]. In this complex, metal ions are connected based on the inorganic layer as a multicomponent nanostructure. After calcination, the layer becomes a mixed-metal-oxide nanostructure.

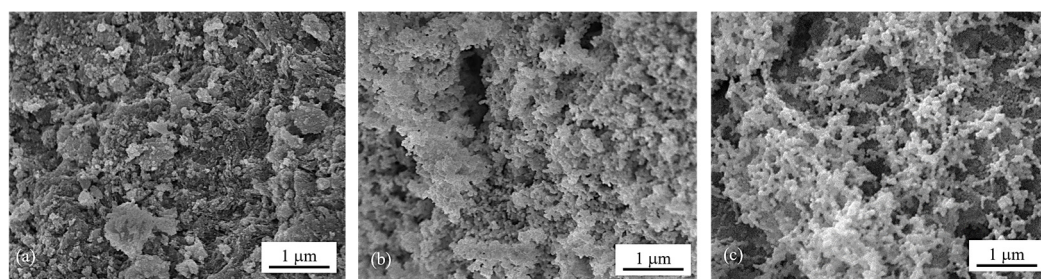


Figure 1. FESEM micrographs of calcined (a) 5Ni5Ce/MA, (b) 5Ni5Ce(6 h)/MA, and (c) 5Ni5Ce(20 h)/MA catalysts.

The textural properties of all samples were examined using N₂ adsorption–desorption measurements. The isotherm patterns of all samples (Figure 2) exhibit a type IV(a) isotherm feature of mesoporous materials with the combination of H2(b) and H3 hysteresis loops (IUPAC), correlating to the connection of the bottleneck-shaped and plate-shaped pores in the relative pressure range (P/P_0) of 0.60–1.00 [25–28]. Using the BJH method, the pore size distribution curves of all samples are established in Figure 3. Table 1 reports the average pore size diameter estimated from the BJH method and the surface area with the total pore volume calculated from the BET equation. The support and catalyst samples show an average pore size diameter smaller than 25.0 nm. The surface of the MA support has an area of 151 m² g^{−1} with an average pore size diameter of 8.0 nm and a total pore volume of 0.52 cm³ g^{−1}. When 5 wt% Ni and 5 wt% CeO₂ were loaded onto the MA support (5Ni5Ce/MA), the surface area decreased to 108 m² g^{−1} with a total pore volume of 0.51 cm³ g^{−1}, whereas the average pore size diameter increased to 10.8 nm. These results can be explained by the blockage of smaller pores of the MA support by large nanoparticles [29,30]. Considering the ammonia vapor diffusion impregnation of 5 wt% Ni and 5 wt% CeO₂ for 6 h (5Ni5Ce(6 h)/MA) and 20 h (5Ni5Ce(20 h)/MA), the surface area and total pore volumes of these two catalysts are similar (101 m² g^{−1} and 0.43–0.44 cm³ g^{−1}, respectively). These values of the textural properties are lower than 5Ni5Ce/MA due to the stronger blocking effect caused by the growth of the mixed-oxide nanoparticles.

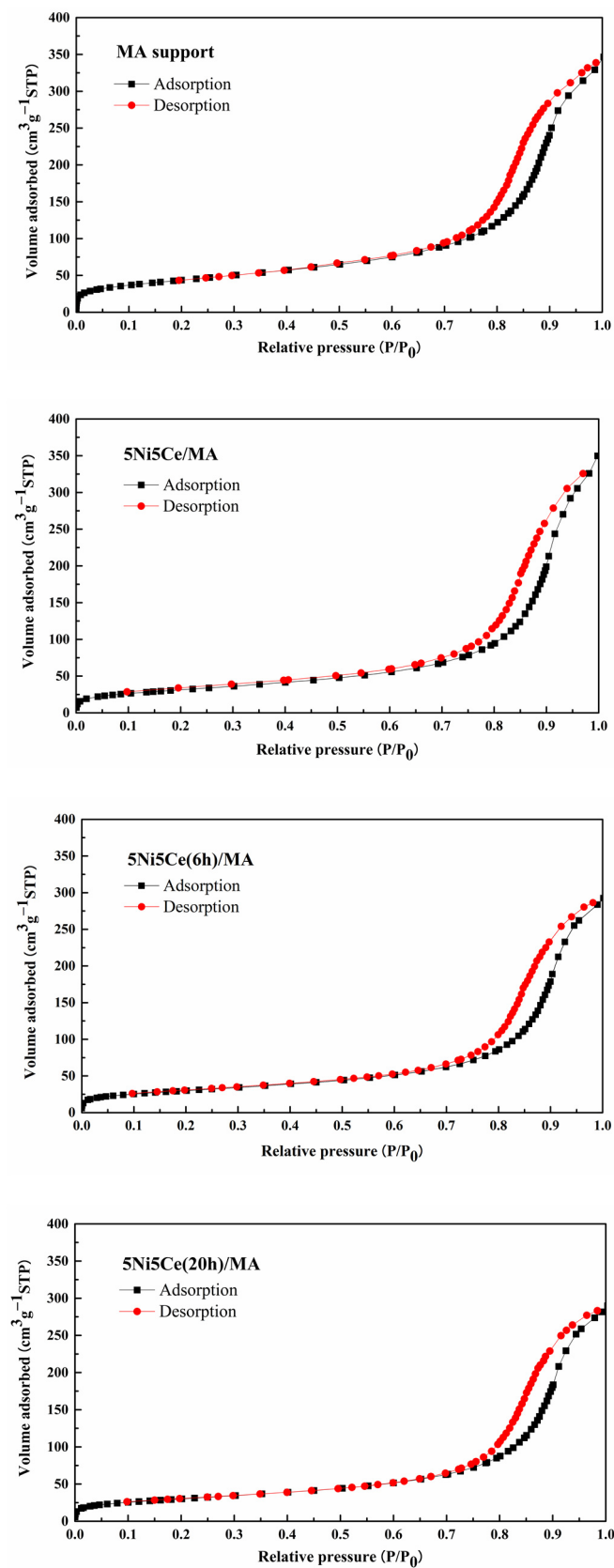


Figure 2. N₂ adsorption–desorption isotherms of support and all calcined catalysts.

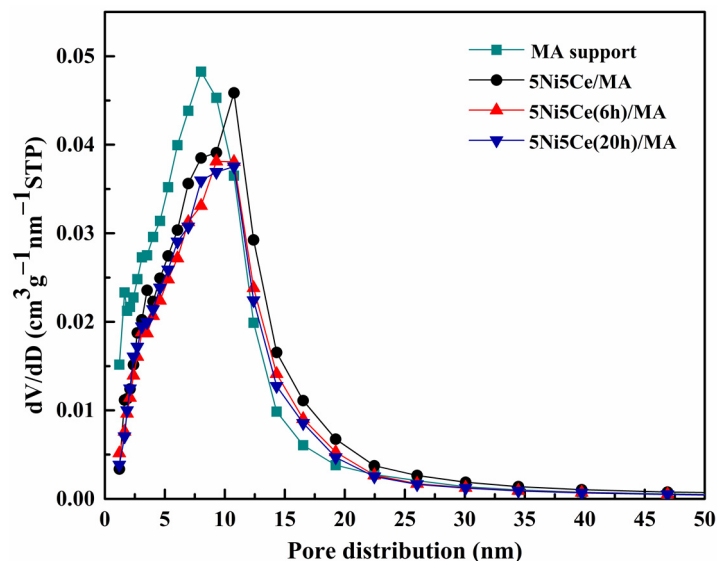


Figure 3. BJH pore size distributions of support and all calcined catalysts.

Table 1. Bulk and surface properties of support and all calcined catalysts.

Sample	Surface Area (m ² g ^{−1})	Total Pore Volume (cm ³ g ^{−1})	Average Pore Diameter (nm) ^a	Crystallite Size of CeO ₂ (nm) ^b
MgO-Al ₂ O ₃	151	0.52	8.0	-
5Ni5Ce/MA	108	0.51	10.8	6.7
5Ni5Ce(6 h)/MA	101	0.44	9.3	5.4
5Ni5Ce(20 h)/MA	101	0.43	10.8	7.2

^a Average pore diameter determined by BJH model. ^b Crystallite size of CeO₂ calculated by Scherrer's equation.

The X-ray diffraction patterns of the MA support, calcined catalysts, and reduced catalysts are presented in Figure 4. According to Figure 4a, the diffractogram of the MA support represents the peak patterns of the MgAl hydrotalcite phase (JCPDS No. 022-0700) and the MgAl₂O₄ spinel structure (JCPDS No. 01-084-0377) [31–34]. After calcination in the catalyst preparation, the MgAl hydrotalcite phase is completely transformed into the MgAl₂O₄ spinel phase, as the pattern of MgAl hydrotalcite cannot be observed in the diffractograms of the calcined catalysts (Figure 4a). When the 5 wt.% Ni and 5 wt.% CeO₂ were impregnated onto the MA support, the pattern of the spinel phase could also be attributed to the occurrence of NiAl₂O₄ (JCPDS No. 10-0339) on all of the calcined catalysts. This pattern overlaps with the diffraction peaks of MgAl₂O₄ spinel and NiO crystalline phase (JCPDS No. 47-1049). Likewise, nickel oxide phases and the nickel metal phase (JCPDS No. 04-0850) are seldom identified in the diffractograms of the reduced catalysts (Figure 4b) due to the overlapping peaks in the patterns of various nickel crystalline systems [35–37]. Thus, the nickel species on the reduced catalysts were investigated via XPS characterization. Differently, the peak patterns of CeO₂ (JCPDS No. 43-1002) were detected in the diffractograms of all the calcined catalysts and reduced catalysts [38–41]. For a quantitative comparison, the CeO₂ crystallite sizes on the calcined catalysts (Table 1) were determined via Scherrer's equation at 2 theta = 28°. Compared to the calcined 5Ni5Ce/MA, the average CeO₂ crystallite size slightly decreased when the catalyst was treated in ammonia vapor for 6 h, indicating a greater distribution of the NiO-CeO₂ nanostructure. Contrarily, the crystallite size of CeO₂ on the surface increased when the catalyst was treated in ammonia vapor for 20 h, implying the growth of a mixed-metal-oxide nanostructure during the time of treatment. Although the crystallite sizes of CeO₂ on the reduced catalysts were smaller than those of the calcined catalysts due to

the partial reduction in CeO_2 , the same CeO_2 crystallite size trend was observed on the reduced catalysts.

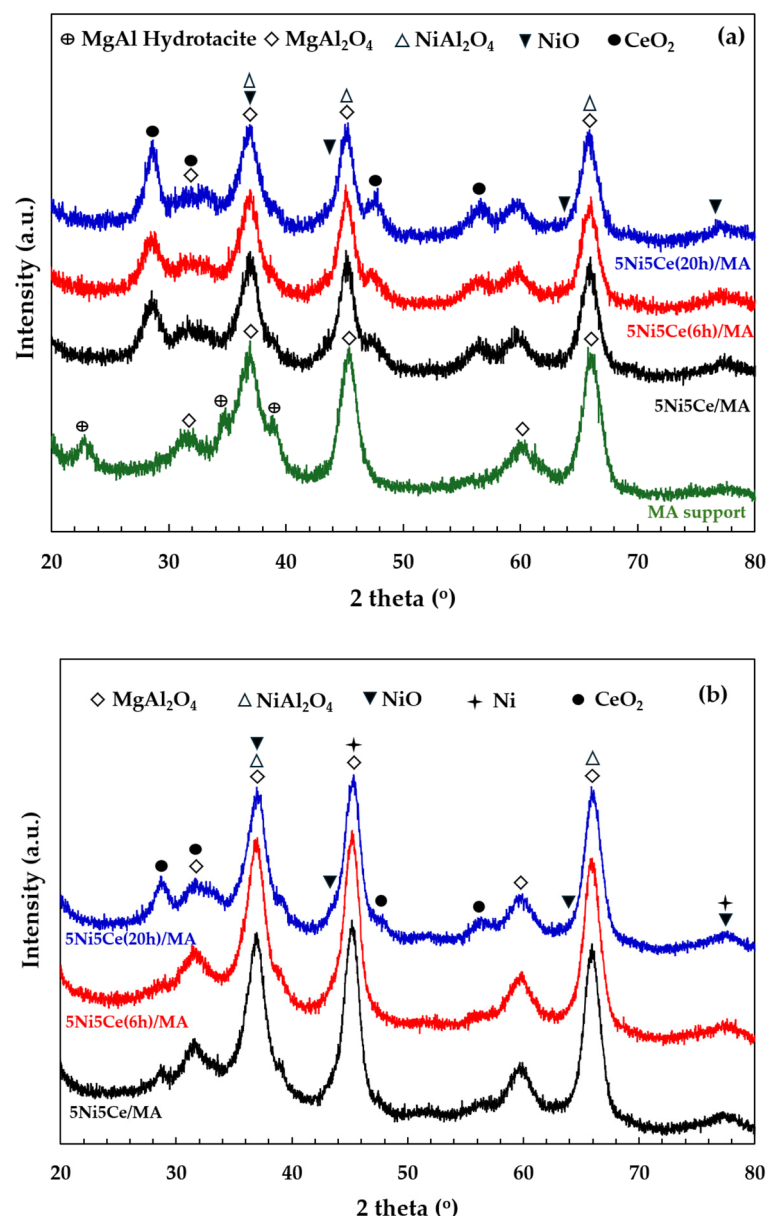


Figure 4. The X-ray diffraction patterns of (a) MA support and calcined catalysts, and (b) reduced catalysts.

2.2. Chemical Properties

The reduction profiles of the oxide species (Figure 5) were carried out by the H_2 temperature program reduction (H_2 -TPR) to determine the reducibility and the interaction among the components of the calcined catalysts. The H_2 -TPR profiles of all the calcined catalysts demonstrate two temperature reduction ranges. The reductions at lower temperature ranging from 250 °C to 450 °C correspond to the NiO species poorly interacting with other components and the partial reduction in CeO_2 . The reduction peaks at temperatures higher than 500 °C are assigned to the moderate-to-strong interaction of NiO- CeO_2 and NiO- CeO_2 -MA and the formation of spinel oxides such as NiAl_2O_4 due to the strong metal-support interaction (SMSI) effect [42–47]. The XPS spectra of Ni 2p + Ce 3d (Figure 6a) and O 1s (Figure 6b) were obtained to investigate the chemical states of Ni and Ce on the surface of all ex situ reduced catalysts. In Figure 6a, the Ni 2p core level spectra show the presence of metallic Ni (Ni^0) at a binding energy (BE) of 851.7–852.9 eV, and Ni^{2+} at a BE

of 855.2–855.9 eV. The Ce 3d core level spectra show the co-existence of Ce^{4+} (blue peaks = v, v'', v''', u, u'', and u''') and Ce^{3+} (blue peaks = v₀, v', u₀, and u') [48–51]. The O 1s peak (Figure 6b) was deconvoluted to identify the oxygen species of the reduced catalysts. The peaks of lattice oxygen (O_{latt}) in NiO, CeO_2 , NiAl_2O_4 , and the MA support was found at a BE of about 530 eV. The peaks of surface oxygen (O_{sur}) based on oxygen vacancies and hydroxyl were observed at higher BE values (531–532 eV) [52,53]. The relative concentration of metallic nickel Ni ($[\text{Ni}^0]/[\text{Ni}^0] + [\text{Ni}^{2+}]$), the relative concentration of Ce^{3+} ($[\text{Ce}^{3+}]/[\text{Ce}^{4+}] + [\text{Ce}^{3+}]$), and the $\text{O}_{\text{sur}}/\text{O}_{\text{latt}}$ ratio were then evaluated from their peak areas (Table 2).

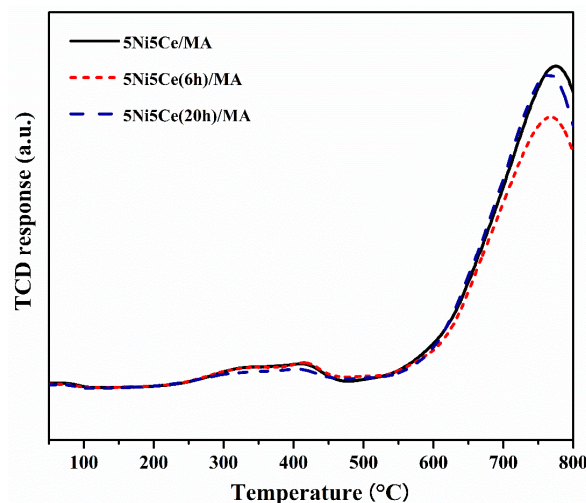


Figure 5. H_2 -TPR profiles of all reduced catalysts.

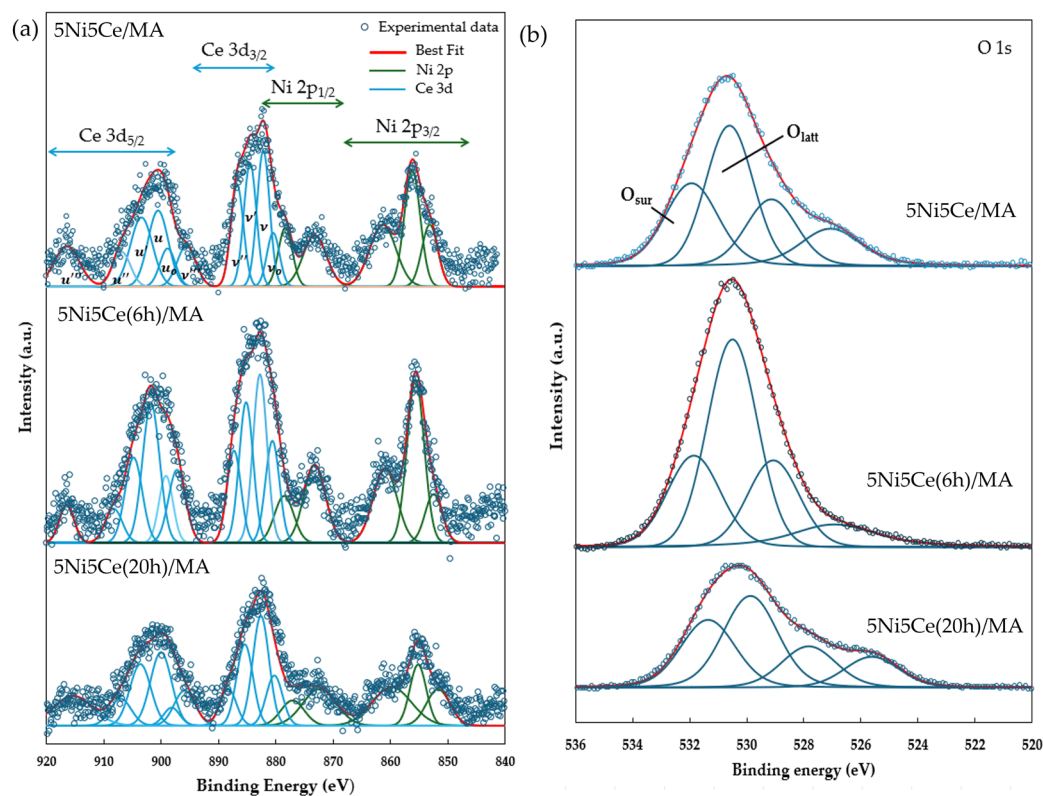


Figure 6. XPS core level spectra of reduced catalysts in (a) Ni 2p + Ce 3d energy region and (b) O 1s energy region.

Table 2. Chemical state analysis of Ni 2p, Ce 3d, and O 1s from XPS spectra.

Samples	$\frac{[\text{Ni}^0]}{[\text{Ni}^0] + [\text{Ni}^{2+}]}$	$\frac{[\text{Ce}^{3+}]}{[\text{Ce}^{3+}] + [\text{Ce}^{4+}]}$	$\text{O}_{\text{sur}}/\text{O}_{\text{latt}}$
5Ni5Ce/MA	0.45	31.30	0.88
5Ni5Ce(6 h)/MA	0.22	28.30	0.47
5Ni5Ce(20 h)/MA	0.29	25.61	0.52

According to the H₂-TPR profiles and XPS results, the maximum hydrogen consumption with the reduction curve at the highest temperature and the maximum relative concentrations of Ni⁰ and Ce³⁺ with the highest O_{sur}/O_{latt} ratio were obtained from the untreated 5Ni5Ce/MA catalyst. These results indicate the greatest reductions in nickel oxide (NiO or NiAl₂O₄ → Ni⁰) and CeO₂ (CeO₂ (Ce⁴⁺) → Ce₂O₃ (Ce³⁺), generating oxygen vacancies) with the presence of spinel phases due to the SMSI effect on the surface of the untreated 5Ni5Ce/MA catalyst. The reduction peak slightly shifts to a lower temperature with the minimum hydrogen consumption on 5Ni5Ce(6 h)/MA. The smallest amount of nickel oxide reduction was confirmed by the lowest Ni⁰ fraction with the lower partial CeO₂ reduction (XPS result). This is owing to the high dispersion of the initiated NiO-CeO₂ nanoparticles on the MA support during the short treatment process. Therefore, the SMSI effect still presents, and the tiny nanoparticles cause some nickel oxide particles to merge completely into the MA support underneath the surface with the NiO-CeO₂ interaction. Consequently, these deduct the reductions in nickel oxide as well as in CeO₂ and show a greater O_{latt} portion on the surface. When treated by ammonia vapor a for longer time (5Ni5Ce(20 h)/MA catalyst), the NiO-CeO₂ network (SEM image) constructed on the surface increases nickel oxide in the mixed-oxide nanoparticles and decreases the isolated CeO₂. Compared to 5Ni5Ce(6 h)/MA, hydrogen consumption at a high temperature range and the relative concentration of Ni⁰ increases while the relative concentration of Ce³⁺ decreases on 5Ni5Ce(20 h)/MA. Considering the quantity of Ni⁰, the hydrogen consumption profiles of H₂-TPR of 5Ni5Ce/MA and 5Ni5Ce(20 h)/MA are almost similar, while the Ni⁰ relative concentrations are different. This indicates the number of Ni²⁺ in other forms. For the treated catalyst with which the surface was constructed in the LDH formation for a long time, the NiO-CeO₂ mixed oxide increased the Ni²⁺ on the surface, forming Ni(OH)₂ and NiO. Moreover, only NiO at the uppermost level can be reduced. Therefore, 5Ni5Ce(20 h)/MA shows a higher O_{sur}/O_{latt} ratio than that of 5Ni5Ce(6 h)/MA.

The metal particle size distributions, including the metal surface layers of the reduced catalysts, were determined via H₂-TPD measurement. Two desorption temperature ranges were observed in the profiles (Figure 7), suggesting a weak hydrogen chemisorption on the Ni metal at the top layer (temperature lower than 180 °C) and the medium–strong hydrogen chemisorption on the Ni metal interacting with the support, contributing to the hydrogen spillover onto the catalyst support (temperatures higher than 180 °C) [54–56]. The amount of hydrogen desorption was determined as reported in Table 3. The H₂-TPD profiles of the reduced catalysts represent different arrangements of Ni metal active sites on the surface. The largest hydrogen desorption at a high temperature range and the smallest hydrogen desorption at a low temperature range were obtained from the untreated catalyst, implying that most Ni metal active sites interacted with the support. The 5Ni5Ce(6 h)/MA catalyst possesses the largest amount of H₂ desorption, representing the highest Ni dispersion. According to the H₂-TPD profiles of the treated catalysts, the hydrogen desorption at high temperature ranges trends to decrease, while the hydrogen desorption at low temperature ranges trends to increase when the duration of the ammonia diffusion treatment increases. These results suggest the raising of the Ni metal active sites on the uppermost surface layer due to the growth of the NiO-CeO₂ layer on the surface, which reduces the interaction of active sites with the support.

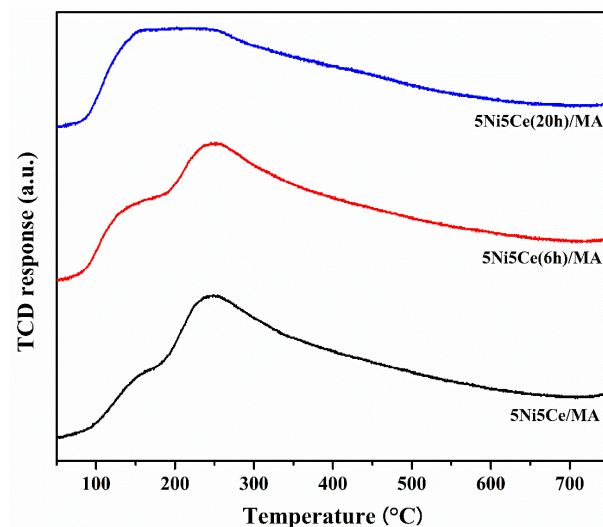


Figure 7. H₂-TPD profiles of all reduced catalysts.

Table 3. The amount of H₂ desorption on all reduced catalysts.

Samples	Amount of H ₂ Desorption (mmol g ^{−1})		
	Weak 100–180 °C	Medium–Strong 180–750 °C	Weak (Medium+Strong)
5Ni5Ce/MA	0.021	0.167	0.126
5Ni5Ce(6 h)/MA	0.032	0.166	0.191
5Ni5Ce(20 h)/MA	0.066	0.123	0.537

The amount and strength of the basic sites on the reduced catalysts related to the catalytic activity of CO₂ were identified by CO₂-TPD (Figure 8). The strength of the basic sites can be distinguished by the temperature corresponding to the desorption of CO₂. The basic sites of reduced 5Ni5Ce/MA, 5Ni5Ce(6 h)/MA, and 5Ni5Ce(20 h)/MA catalysts demonstrate three temperature ranges of CO₂ desorption. The weak basic sites in the low temperature range of 50–150 °C can be ascribed to Brønsted OH[−] groups on the surface, the moderate basic sites (150–400 °C) are attributed to metal–oxygen pairs (Lewis basic site), and the strong basic sites at temperatures higher than 400 °C are assigned to the surface of low coordinated O^{2−} anions [57–59]. Among all the strengths of the basic sites, the Brønsted OH[−] and Lewis basic sites are clearly observed on all reduced catalysts. Table 4 reports the deconvoluted quantities of CO₂ desorption from all reduced catalysts. Accordingly, the treated catalysts present a greater number of Brønsted OH[−] sites than the untreated 5Ni5Ce/MA catalyst, and this type of basic site tends to increase with the duration of treatment. This can be explained by the effect of surface modification by treatment in ammonia vapor diffusion, which composes the surface through the LDH structure and involves the rehydration property (memory effect) after calcination.

Table 4. The amount of CO₂ desorption on all reduced catalysts.

Samples	Amount of CO ₂ Desorption (mmol g ^{−1})			Total Basicity
	Weak 50–150 °C	Moderate 150–400 °C	Strong 400–800 °C	
5Ni5Ce/MA	0.872	1.432	0.643	2.947
5Ni5Ce(6 h)/MA	0.918	1.396	0.688	3.002
5Ni5Ce(20 h)/MA	0.964	0.973	0.501	2.438

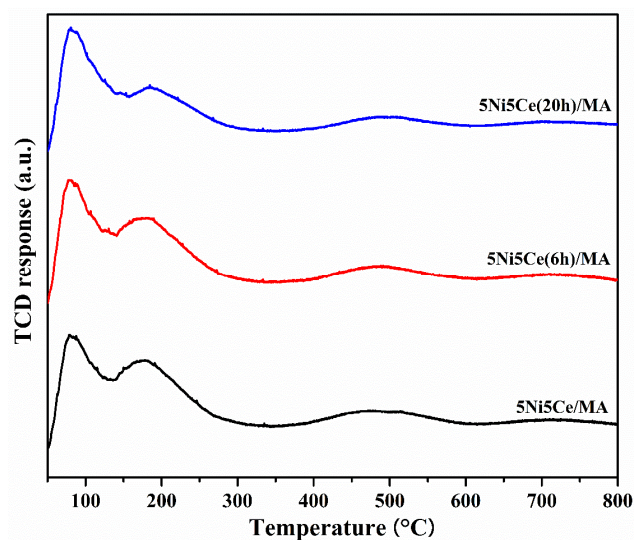


Figure 8. CO₂-TPD profiles of all reduced catalysts.

The oxygen mobility in all reduced catalysts was further evaluated by O₂-TPD measurement (Figure 9) at a temperature range from 50 °C up to 800 °C. The oxygen transfer on the catalyst can be predicted via the O₂-TPD profile. The oxygen desorption peaks at low temperature are assigned to surface oxygen, including physisorbed oxygen molecules and oxygen from oxygen vacancies (resulting from the redox property of Ce⁴⁺/Ce³⁺). At the higher temperature range, the desorption peaks are attributed to lattice oxygen [16,60–65]. The oxygen desorption quantities according to the various types of oxygen mobility were calculated (Table 5). The O₂-TPD results may be relative to the XPS analysis. The 5Ni5Ce/MA catalyst shows two desorption peaks at different ranges of temperature. Compared to 5Ni5Ce/MA, the catalyst treated in the ammonia vapor for 6 h (5Ni5Ce(6 h)/MA catalyst) presents less surface oxygen and more lattice oxygen due to the good dispersion of small NiO-CeO₂ nanoparticles initiated on the surface. For the comparison of treated catalysts (6 h and 20 h), surface oxygen increases, lattice oxygen decreases, and the peaks of surface and lattice oxygen merge smoothly in the O₂-TPD profile of 5Ni5Ce(20 h)/MA. These results indicate the connection of the surface and lattice oxygen through the electronic interaction of Ni-NiO-CeO₂ produced by 20 h ammonia vapor treatment.

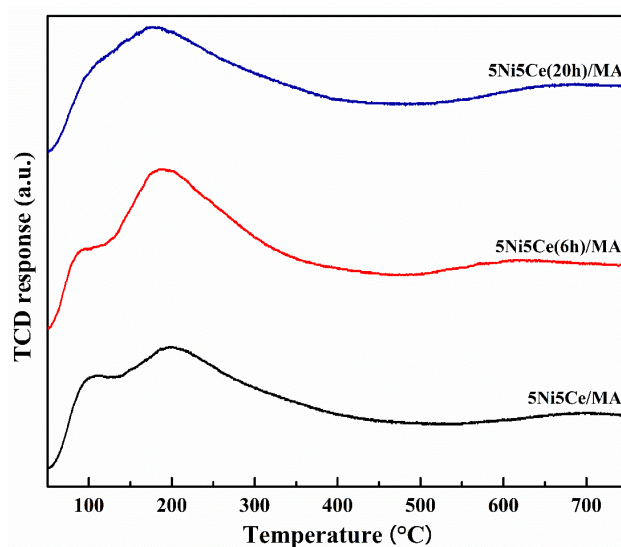


Figure 9. O₂-TPD profiles of all reduced catalysts.

Table 5. The amount of O₂ desorption on all reduced catalysts.

Samples	Amount of O ₂ Desorption (mmol g ^{−1})		
	Surface Oxygen (<150 °C)	Lattice Oxygen (>150 °C)	Total O ₂ Desorption
5Ni5Ce/MA	0.353	1.236	1.589
5Ni5Ce(6 h)/MA	0.259	1.604	1.863
5Ni5Ce(20 h)/MA	0.366	1.051	1.417

2.3. Catalytic Performance and Coke Resistance

The CMR catalytic behaviors of the 5Ni5Ce/MA and treated 5Ni5Ce(xh)/MA catalysts were investigated at 600 °C under atmospheric pressure for 16 h. The performance was evaluated by means of CH₄ conversion, CO₂ conversion, and the H₂/CO ratio of the syngas product (Figure 10). The 5Ni5Ce/MA catalyst presents an average CH₄ conversion of 59.4%, an average CO₂ conversion of 43.5%, and a H₂/CO ratio of 0.58 (H₂ yield = 51.8% and CO yield = 82.7%). Compared to 5Ni5Ce/MA, the 5Ni5Ce(6h)/MA catalyst reflects the relative higher activity toward CH₄ conversion (68.8%) and CO₂ conversion (47.9%) with similar H₂/CO ratio of 0.56 (H₂ yield = 54.8% and CO yield = 90.9%). The highest CH₄ conversion of 72.2%, the highest CO₂ conversion of 52.1%, and a H₂/CO ratio of 0.59 (H₂ yield = 62.3% and CO yield = 95.3%) were obtained from the 5Ni5Ce(20h)/MA catalyst. The enhancement of reactant activities as well as product yields on 5Ni5Ce(20h)/MA can be attributed to the number of active sites in the Ni-NiO-CeO₂ network. As observed in CO₂-TPD, these Ni-NiO-CeO₂ nanostructures develop their electronic interactions with the nanostructure over the course of treatment. The surface hydroxide on the structure increases the turnover frequency of CO₂ on the Ni-NiO-CeO₂ network, agreeing with the CO₂-TPD measurement. These surface hydroxyl sites allow Ni metal sites to be active toward CH₄. For the CO yield values in which CH₄ and CO₂ consumptions were considered, the treated catalysts had smaller amounts of carbon deposition than the untreated catalyst. The coke deposition analysis is discussed in the following part. Moreover, the highest H₂ yield (62.3%), the highest CO yield (95.3%) and the slightly higher H₂/CO ratio (0.59) observed on the 5Ni5Ce(20 h)/MA catalyst imply a reduced RWGS side reaction effect. This is assigned to the rehydration property promoting H₂O adsorption–dissociation [20].

The carbon deposition on each spent catalyst after the CRM test was analyzed by TPO measurement (Figure 11), FESEM (Figure 12), and XRD (Figure 13). The oxygen consumption curves representing the carbon oxidation profiles of all samples are depicted in Figure 10, and the amount of oxygen consumptions are reported in Table 6. The oxidation peaks in the low-to-medium-temperature (<500 °C) and high-temperature (>500 °C) ranges can be assigned to the combustion of amorphous carbon and graphitic carbon collaborating with filamentous carbon, respectively [16,66–70]. The greatest amount of total oxygen consumption found on the spent 5Ni5Ce/MA suggests the largest amount of coke deposition. It decreased by 30% on the spent 5Ni5Ce(6 h)/MA and decreased by half on the spent 5Ni5Ce(20 h)/MA. Although a large amount of filamentous carbon was spread out over the surface of 5Ni5Ce/MA (Figure 12a–c), this carbon filament on the spent 5Ni5Ce/MA was oxidized easier than the treated catalysts due to the lower oxidation temperature. The XRD diffractograms of the reduced and spent catalysts establish the phase maintained during the reaction with the deposition of graphitic carbon (Figure 13). The XRD diffractograms of the spent catalysts display the peak patterns of graphitic carbon (JCPDS No. 41-1487) only on the treated catalysts [16,71]. This evidence reflects the change in the electronic effect on the nickel–ceria catalyst caused by the ammonia diffusion impregnation method. The electronic interaction of NiO-CeO₂ developed through LDH synthesis generates and grows surface hydroxyl with the oxygen transfer pathway of the Ni-NiO-CeO₂ network. However, it decreases the oxygen vacancies of CeO₂ compared to the reduced 5Ni5Ce/MA catalyst. As a consequent, the reactant cracking, especially CO₂, on 5Ni5Ce/MA is slower

by the metal–oxide pair basic sites and the coke oxidation is driven only by surface oxygen (O^*) from the CO_2 adsorption–dissociation. Moreover, the beneficial pathway of oxygen transfer through the Ni–NiO– CeO_2 network to the deposited carbon rarely takes place on this catalyst. When the 5Ni5Ce/MA catalyst is treated in the ammonia vapor, the reactant cracking becomes faster and more specific onto the appropriate sites as explained above. Thus, graphitic carbon and a thick carbon filament were found on the treated catalysts. The smaller amount of coke deposited on the treated catalysts represents the higher rate of coke removal. This is attributed to the implementation of oxygen transfer into the Ni–NiO– CeO_2 network associated with the rehydration property of Ni–NiO– CeO_2 interactions, indicating more surface hydroxyl (OH^*). Ni–NiO– CeO_2 nanoparticles on 5Ni5Ce(20 h)/MA provide OH^* and O^* to drive the reaction pathways that transform CH^* and C^* to CO^* (Equations (5)–(7)).

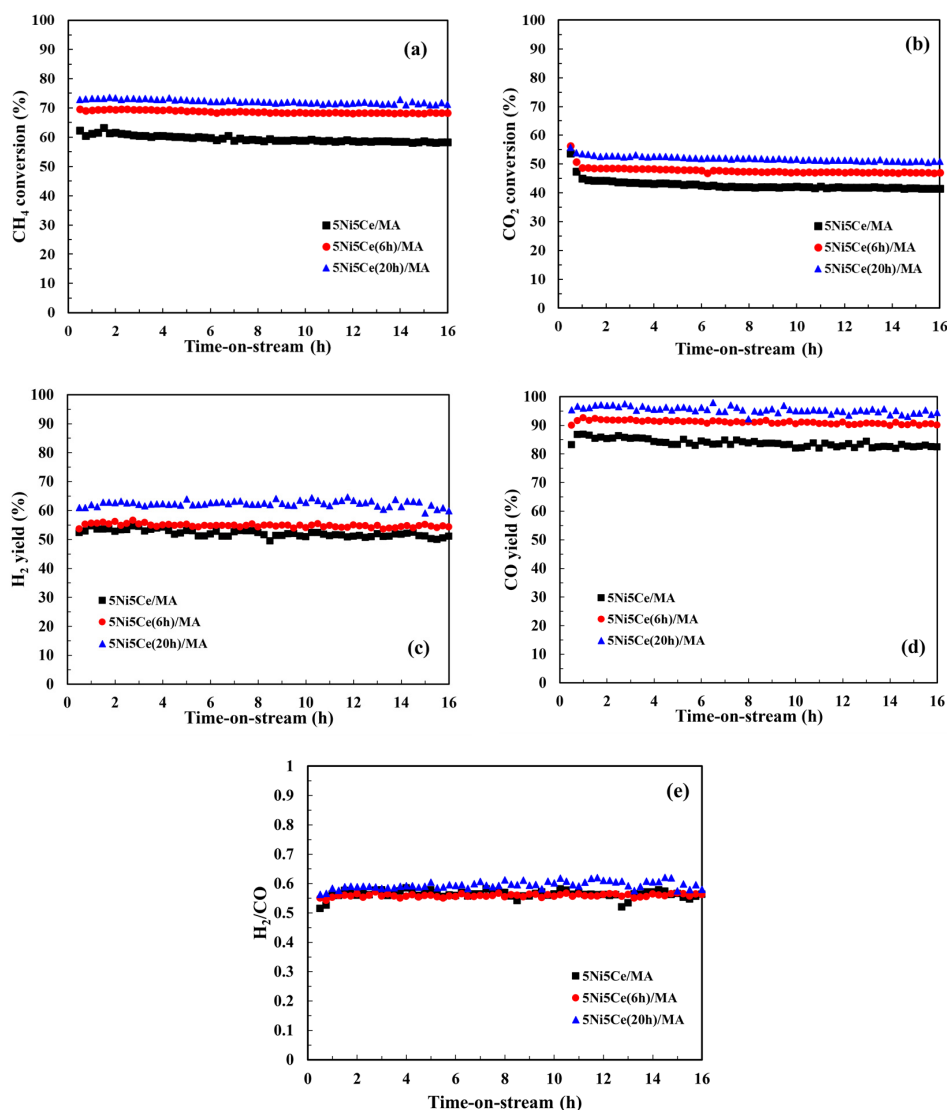
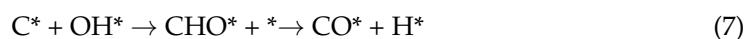
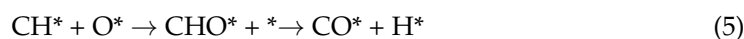


Figure 10. (a) CH_4 conversion, (b) CO_2 conversion, (c) H_2 yield, (d) CO yield, and (e) H_2/CO ratio for the CO_2 reforming of methane (CRM) of all catalysts. Reaction conditions: 600 °C and 1 atm for 16 h.

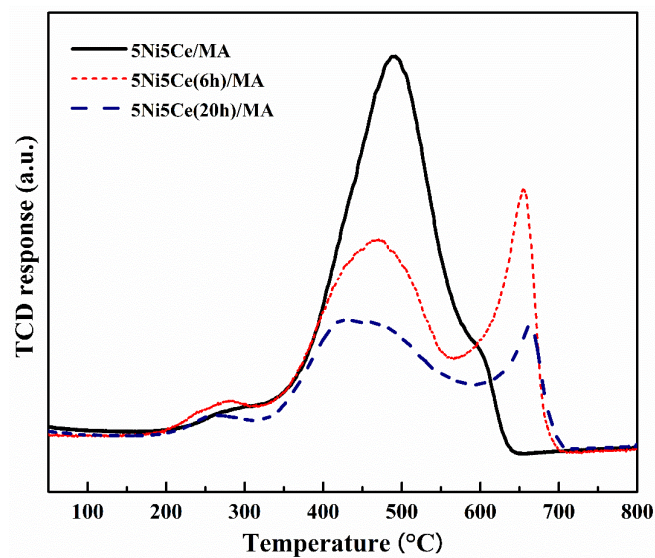


Figure 11. TPO profile of spent catalysts after CRM reaction.

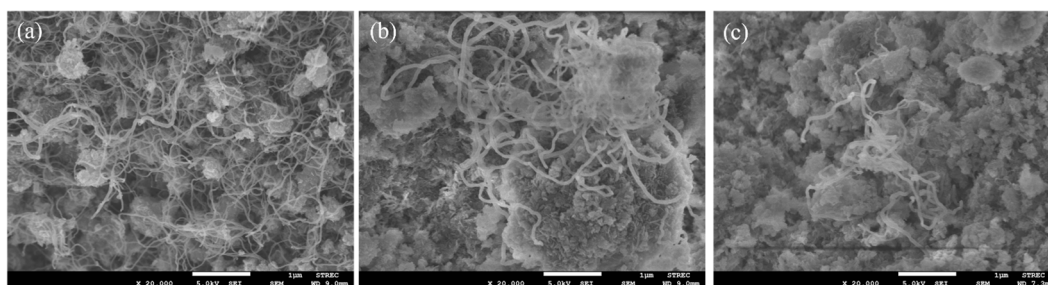


Figure 12. FESEM micrographs of spent (a) 5Ni5Ce/MA, (b) 5Ni5Ce(6 h)/MA, and (c) 5Ni5Ce(20 h)/MA catalysts.

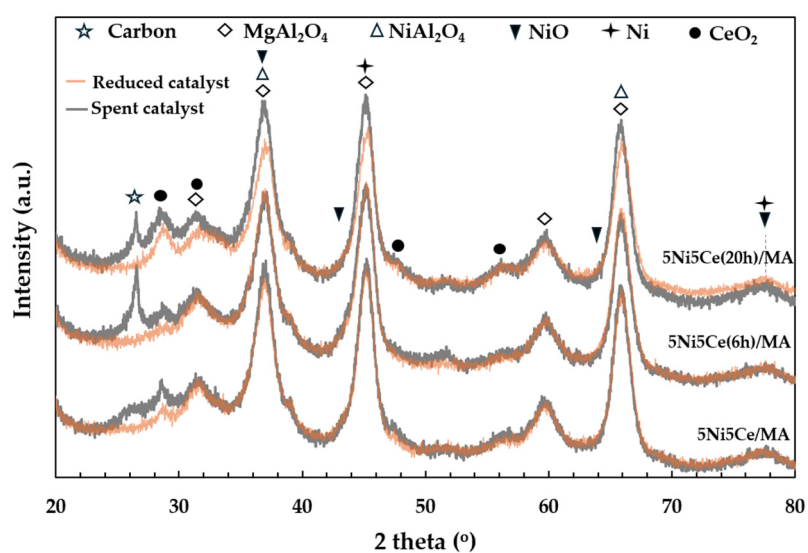


Figure 13. The X-ray diffraction patterns of the reduced catalysts and spent catalysts.

Table 6. The O₂ consumption for carbon oxidation on all spent catalysts.

Samples	O ₂ Consumption (mmol g ^{−1})			Total O ₂ Consumption
	Amorphous Carbon (<320 °C)	Graphitic Carbon (320–550 °C)	Filamentous Carbon (>550 °C)	
5Ni5Ce/MA	0.87	13.53	2.62	17.02
5Ni5Ce(6 h)/MA	0.94	6.11	4.81	11.86
5Ni5Ce(20 h)/MA	0.68	5.21	2.52	8.4

3. Materials and Methods

3.1. Material Preparation

The catalyst support, 10 wt% MgO/Al₂O₃ (MA), was synthesized by incipient wetness impregnation of Al₂O₃ powder (98%, Sigma Aldrich, St. Louis, MO, USA) with an aqueous solution of Mg(NO₃)₂·6H₂O (98%, Acros Organics, Waltham, MA, USA). The wet powder was stabilized in ambient condition for 12 h before being dried at 50 °C overnight and calcined at 650 °C for 6 h. Afterwards, 5 wt% Ni-5 wt% CeO₂/MgO-Al₂O₃ (5Ni5Ce/MA) was prepared through the conventional co-impregnation method. The mixture of the required portion of the Ni(NO₃)₂·6H₂O (98%, Acros Organics) solution and the Ce(NO₃)₃·6H₂O (98%, Sigma Aldrich) solution was dropped onto the MA support followed by drying at 50 °C overnight and calcination at 650 °C for 6 h.

To generate two treated catalysts with various interactions on the surface, the 5Ni5Ce(xh)/MA (xh = 6 h and 20 h) catalysts were synthesized using an ammonia vapor diffusion impregnation method outlined in our previous work [19]. The wet solid cake of the impregnated 5Ni5Ce/MA catalyst was kept under ammonia vapor diffusion conditions at ambient temperature in a closed chamber for 6 h (5Ni5Ce(6 h)/MA) and for 20 h (5Ni5Ce(20 h)/MA). During the ammonia diffusion, a limited amount of hydroxide ions was intercalated with the nitrate ions of the Ni²⁺ and Ce³⁺ solutions, resulting in the slow growth of the layered double hydroxide nanosheet structure. Hence, the size and dispersion of the layered double hydroxide nanosheets were controlled by diffusion time. The resulting wet powder was dried and calcined using similar conditions to those used for the 5Ni5Ce/MA catalyst. All catalysts were pelletized, ground, and sieved to a particle size range between 355 and 710 µm.

3.2. Material Characterization

The surface morphologies of the calcined and spent catalysts were characterized by field emission scanning electron microscopy (FESEM) using the JEOL instrument model JSM-7610F (JEOL Ltd., Welwyn Garden City, UK) with an accelerating voltage of 1.00 kV. Prior to the analyzation, each catalyst sample was prepared by sputter coating with platinum (Pt) using a QUORUM Q150R S (Quorum, East Sussex, UK) apparatus.

The surface area and pore properties of the catalyst were obtained using the N₂ adsorption–desorption isotherm measured at −196 °C on an Autosorb iQ Station 2 (Quantachrome Instruments, Boynton Beach, FL, USA). Prior to the experiment, the catalyst was outgassed at 350 °C under a N₂ flow for 3 h. The surface area and the total pore volume were analyzed by multipoint Brunauer–Emmett–Teller (BET) method. The average pore diameter was calculated from the Barrett–Joyner–Halenda (BJH) method.

The crystalline phase compositions of the prepared support, calcined catalysts, reduced catalysts, and spent catalysts were identified by X-ray diffraction (XRD, Bruker AXS Model D8 Discover, Billerica, MA, USA) with CuKα radiation at 40 kV and 40 mA and recorded in 2 theta ranges of 10–80° with the step size of 0.02° min^{−1}. The average crystallite sizes (D_{XRD}) on the fresh catalysts were calculated from the values of full width at half maximum (FWHM) of the intense diffraction peak at 2 theta = 28° for CeO₂ using Scherrer's equation

(Equation (8)), where K is the particle shape factor (0.94), λ is 1.5418 Å, β is line broadening in radians, and θ is the Bragg angle.

$$D(\text{XRD}) = \frac{K\lambda}{\beta \cos \theta} \quad (8)$$

The reducibility of the calcined catalysts was analyzed by hydrogen temperature-programmed reduction (H_2 -TPR) measurements performed on a BELCAT basic system (BEL JAPAN, INC., Osaka, Japan) using a thermal conductivity detector (TCD). A total of 0.050 g of each sample was first degassed with Ar flow at 220 °C for 1.5 h, and cooled down to 40 °C. In the measurement, the sample was reduced in the reducing gas flow (5 vol% H_2 /Ar, 30 mL min^{−1}) from 50 °C to 800 °C with a ramping rate of 10 °C min^{−1}. The water vapor from the gas stream was removed using a molecular sieve 4A, and the hydrogen consumption was examined by the TCD equipped in the analyzer.

The chemical states of Ni and Ce in the reduced catalysts were investigated by X-ray photoelectron spectroscopy (XPS) measurement, employing a PHI5000 Versa Probe II (ULVAC-PHI, Chigasaki, Japan). Prior to the measurement, catalysts were reduced ex situ at 600 °C for 3 h under pure H_2 . The monochromatic $\text{AlK}\alpha$ X-ray (1486.6 eV) was utilized as an excitation source. The C 1s BE at 285.0 eV was used as a reference for calibration. The high-resolution XPS spectra were collected with an energy step of 0.1 eV and pass energy of 46.95 eV. After measurement, XPS spectra were analyzed using the CasaXPS software (version 2.3.26).

The dispersion of metal active sites was investigated via H_2 temperature-programmed desorption (H_2 -TPD) measured on the BELCAT basic system. Firstly, the catalyst sample (0.050 g) was pre-treated in Ar flow (30 mL min^{−1}) at 220 °C for 1 h, reduced in situ with pure H_2 flow (30 mL min^{−1}) at 600 °C for 1.5 h, and cooled to 120 °C in Ar flow. After that, the H_2 adsorption on the reduced catalyst was carried out in pure H_2 flow at 120 °C for 1 h. The physisorbed H_2 was purged with Ar flow for 1 h, and the sample was cooled to 50 °C. Finally, the H_2 -TPD measurement was performed from 50 °C to 850 °C at the heating rate of 10 °C min^{−1} in Ar flow.

The surface alkalinity and basic strength distribution of the reduced catalysts were evaluated by CO_2 temperature-programmed desorption (CO_2 -TPD) conducted on the same BELCAT apparatus. Prior to the experiment, the catalyst sample was pre-treated in He flow (30 mL min^{−1}) at 220 °C for 1 h, and reduced in situ with pure H_2 flow (30 mL min^{−1}) at 600 °C for 1.5 h. The sample was thereafter cooled to 40 °C in He flow, and an isothermal CO_2 adsorption was subsequently introduced to the catalyst surface at 40 °C for 1 h. The unadsorbed CO_2 was removed by flushing with He flow for 1 h. Then, the CO_2 desorption was measured with a heating rate of 10 °C min^{−1} to 800 °C in He flow.

The total amount of oxygen mobility and the distribution of the mobile species were determined via temperature-programmed desorption of oxygen (O_2 -TPD) on the same BELCAT instrument (Microtrac, York, PA, USA). Before the O_2 adsorption step, the catalyst sample was pre-treated and pre-reduced in situ under the same conditions as H_2 -TPD. The sample was cooled to 200 °C in Ar flow. Afterward, O_2 adsorption on the reduced catalyst was carried out in pure O_2 flow at 200 °C for 1.5 h and the physisorbed O_2 was removed with Ar flow. Then, the desorption was monitored from 50 °C to 800 °C at a heating rate of 10 °C min^{−1} in Ar flow.

The total carbon deposition and carbon type distribution on the spent catalysts after the CRM reaction test were elucidated by temperature-programmed oxidation (TPO) using the BELCAT basic system. A total of 0.050 g of each spent catalyst was cleaned in Ar flow (30 mL min^{−1}) at 220 °C for 2 h, followed by cooling to 40 °C before the TPO measurement. Then, the cleaned sample was oxidized in a 5 vol.% O_2 /Ar flow (30 mL min^{−1}) with a ramping rate of 10 °C min^{−1} from 50 °C to 800 °C. The CO_2 product that evolved from the catalyst surface was removed by a 4A molecular sieve and the oxygen consumption was determined by the TCD equipped in the analyzer.

3.3. Catalytic Performance Tests

The CRM was tested in a tubular reactor at 600 °C under atmospheric pressure for 16 h. Prior to each test, a 350 mg catalyst sample was reduced in situ under H₂ flow (30 mL min^{−1}) at 600 °C for 3 h. Then, the reaction feedstock of a CH₄:CO₂:N₂ mixture with a molar ratio of 3:5:4 at the total flow rate of 60 mL min^{−1} was introduced into the reactor. The composition of the outlet stream was analyzed using an on-line gas chromatograph (Agilent GC7890A, Santa Clara, CA, USA) equipped with a TCD. The reactant conversions (Equations (9) and (10)), product yields (Equations (11) and (12)), and H₂/CO ratio (Equation (13)) were calculated by the equations below.

$$\%CH_4 \text{ conversion} = \frac{\Delta \text{Flow rate of } CH_4}{\text{Flow rate of } CH_{4,in}} \times 100 \quad (9)$$

$$\%CO_2 \text{ conversion} = \frac{\Delta \text{Flow rate of } CO_{2,in}}{\text{Flow rate of } CO_{2,in}} \times 100 \quad (10)$$

$$\%H_2 \text{ yield} = \frac{\text{Flow rate of } H_{2,out}}{2(\Delta \text{Flow rate of } CH_4)} \times 100 \quad (11)$$

$$\%CO \text{ yield} = \frac{\text{Flow rate of } CO_{out}}{\Delta \text{Flow rate of } CH_4 + \Delta \text{Flow rate of } CO_2} \times 100 \quad (12)$$

$$\frac{H_2}{CO} \text{ ratio} = \frac{\text{Flow rate of } H_{2,out}}{\text{Flow rate of } CO_{out}} \quad (13)$$

4. Conclusions

This study discloses the effect of the growth of Ni-NiO-CeO₂ nanoparticles on 5 wt% Ni-5 wt% CeO₂/MA (treated) catalyst employing impregnation-assisted ammonia vapor diffusion for 6 h and 20 h. Compared to the untreated 5 wt% Ni-5 wt% CeO₂/MA, the growth of Ni-NiO-CeO₂ nanoparticles constructed a Ni-NiO-CeO₂ network on the MA support with electronic interaction. The short duration of ammonia vapor diffusion initiates the electronic interaction of Ni-NiO-CeO₂, interrupts strong metal-support interaction, creates a high dispersion of small Ni-NiO-CeO₂ nanoparticles, and increases surface hydroxyl basic sites. A stronger interaction in the Ni-NiO-CeO₂ network is developed over the ammonia diffusion time. Ni metal and the surface hydroxyl sites on Ni-NiO-CeO₂ nanostructures with lower metal-support interaction raise catalytic activities toward involving a drastic reactant dissociation. Although the hard removal types of coke are formed on treated catalysts, the rate of coke oxidation is dramatically driven by mobile O* and OH* in strong Ni-NiO-CeO₂ interactions.

Author Contributions: Conceptualization, M.P. and S.T.; methodology, M.P., S.T., S.I., and W.S.; validation, M.P., S.T. and S.I.; formal analysis, M.P., S.T., S.I., W.S., and T.R.; investigation, M.P.; resources, M.P.; data curation, M.P. and S.T.; writing—original draft preparation, M.P., S.T., and S.I.; writing—review and editing, M.P. and S.T.; visualization, M.P.; supervision, M.P.; project administration, M.P.; funding acquisition, M.P. All authors have read and agreed to the published version of the manuscript.

Funding: This research was funded by the National Science, Research, and Innovation Fund (NSRF) and King Mongkut's University of Technology North Bangkok with Contract no. KMUTNB-FF-66-25.

Institutional Review Board Statement: Not applicable.

Informed Consent Statement: Not applicable.

Data Availability Statement: Data are contained within the article.

Acknowledgments: This work was supported by the National Science, Research, and Innovation Fund (NSRF) and King Mongkut's University of Technology North Bangkok under research grant number KMUTNB-FF-66-25. The XPS measurements were performed at the SUT-NANOTEC-SLRI joint research facility of the Synchrotron Light Research Institute (SLRI), Thailand.

Conflicts of Interest: The authors declare no potential conflicts of interest with respect to the research, authorship, and/or publication of this article.

References

- Li, R.; Gao, T.; Wang, Y.; Chen, Y.; Luo, W.; Wu, Y.; Zhang, Y. Engineering of bimetallic Au–Pd alloyed particles on nitrogen defects riched g-C₃N₄ for efficient photocatalytic hydrogen production. *Int. J. Hydrogen Energy* **2024**, *63*, 1116–1127. [\[CrossRef\]](#)
- Cao, Y.; Fang, H.; Guo, C.; Sun, W.; Xu, Y.; Wu, Y.; Wang, Y. Alkynyl boosted high-performance lithium storage and mechanism in covalent phenanthroline framework. *Angew. Chem. Int. Ed.* **2023**, *62*, e202302143. [\[CrossRef\]](#)
- Arora, S.; Prasad, R. An overview on dry reforming of methane: Strategies to reduce carbonaceous deactivation of catalysts. *RSC Adv.* **2016**, *6*, 108668–108688. [\[CrossRef\]](#)
- Zhang, X.; Zhang, Q.; Tsubaki, N.; Tan, Y.; Han, Y. Carbon dioxide reforming of methane over Ni nanoparticles incorporated into mesoporous amorphous ZrO₂ matrix. *Fuel* **2015**, *147*, 243–252. [\[CrossRef\]](#)
- Zhang, X.; Wang, F.; Song, Z.; Zhang, S. Comparison of carbon deposition features between Ni/ZrO₂ and Ni/SBA-15 for the dry reforming of methane Reaction Kinetics. *Mech. Catal.* **2020**, *129*, 457–470.
- Ye, R.P.; Gong, W.; Sun, Z.; Sheng, Q.; Shi, X.; Wang, T.; Yao, Y.G. Enhanced stability of Ni/SiO₂ catalyst for CO₂ methanation: Derived from nickel phyllosilicate with strong metal-support interactions. *Energy* **2019**, *188*, 116059. [\[CrossRef\]](#)
- Yan, X.U.; Du, X.H.; Jing, L.L.; Peng, W.A.; Jie, Z.H.; Ge, F.J.; Jun, Z.H.; Ming, S.O.; Zhu, W.Y. A comparison of Al₂O₃ and SiO₂ supported Ni-based catalysts in their performance for the dry reforming of methane. *J. Fuel Chem. Technol.* **2019**, *47*, 199–208.
- Arman, A.; Hagos, F.Y.; Abdullah, A.A.; Mamat, R.; Aziz, A.R.A.; Cheng, C.K. Syngas production through steam and CO₂ reforming of methane over Ni-based catalyst-A Review. *IOP Conf. Ser. Mater. Sci. Eng.* **2020**, *736*, 042032. [\[CrossRef\]](#)
- Wei, M.; Shi, X. Research Progress on Stability Control on Ni-Based Catalysts for Methane Dry Reforming. *Methane* **2024**, *3*, 86–102. [\[CrossRef\]](#)
- Mohanty, U.S.; Ali, M.; Azhar, M.R.; Al-Yaseri, A.; Keshavarz, A.; Iglauer, S. Current advances in syngas (CO + H₂) production through bi-reforming of methane using various catalysts: A review. *Int. J. Hydrogen Energy* **2021**, *46*, 32809–32845. [\[CrossRef\]](#)
- Deng, H.; Guo, Y. Artificial Neural Network Model for the Prediction of Methane Bi-Reforming Products Using CO₂ and Steam. *Processes* **2022**, *10*, 1052. [\[CrossRef\]](#)
- Kim, M.J.; Youn, J.R.; Kim, H.J.; Seo, M.W.; Lee, D.; Go, K.S.; Jeon, S.G. Effect of surface properties controlled by Ce addition on CO₂ methanation over Ni/Ce/Al₂O₃ catalyst. *Int. J. Hydrogen Energy* **2020**, *45*, 24595–24603. [\[CrossRef\]](#)
- Rad, S.J.H.; Haghighi, M.; Eslami, A.A.; Rahmani, F.; Rahemi, N. Sol–gel vs. impregnation preparation of MgO and CeO₂ doped Ni/Al₂O₃ nanocatalysts used in dry reforming of methane: Effect of process conditions, synthesis method and support composition. *Int. J. Hydrogen Energy* **2016**, *41*, 5335–5350.
- Moogi, S.; Lee, I.G.; Hwang, K.R. Catalytic steam reforming of glycerol over Ni–La₂O₃–CeO₂/SBA-15 catalyst for stable hydrogen-rich gas production. *Int. J. Hydrogen Energy* **2020**, *45*, 28462–28475. [\[CrossRef\]](#)
- Aghamohammadi, S.; Haghighi, M.; Maleki, M.; Rahemi, N. Sequential impregnation vs. sol-gel synthesized Ni/Al₂O₃–CeO₂ nanocatalyst for dry reforming of methane: Effect of synthesis method and support promotion. *Mol. Catal.* **2017**, *431*, 39–48. [\[CrossRef\]](#)
- Luisetto, I.; Tuti, S.; Battocchio, C.; Lo Mastro, S.; Sodo, A. Ni/CeO₂–Al₂O₃ catalysts for the dry reforming of methane: The effect of CeAlO₃ content and nickel crystallite size on catalytic activity and coke resistance. *Appl. Catal. A Gen.* **2015**, *500*, 12–22. [\[CrossRef\]](#)
- Ismail, A.; Zahid, M.; Hu, B.; Khan, A.; Ali, N.; Zhu, Y. Effect of Morphology-Dependent Oxygen Vacancies of CeO₂ on the Catalytic Oxidation of Toluene. *Catalysts* **2022**, *12*, 1034. [\[CrossRef\]](#)
- Damyanova, S.; Pawelec, B.; Palcheva, R.; Karakirova, Y.; Sanchez, M.C.; Tyuliev, G.; Fierro, J.L.G. Structure and surface properties of ceria-modified Ni-based catalysts for hydrogen production. *Appl. Catal. B Environ.* **2018**, *225*, 340–353. [\[CrossRef\]](#)
- Dharmasaroja, N.; Ratana, T.; Tungkamani, S.; Sornchamni, T.; Simakov, D.S.A.; Phongakorn, M. CO₂ reforming of methane over the growth of hierarchical Ni nanosheets/Al₂O₃–MgO synthesized via the ammonia vapour diffusion impregnation. *Can. J. Chem. Eng.* **2020**, *99*, S585–S595. [\[CrossRef\]](#)
- Sumarasingha, W.; Tungkamani, S.; Ratana, T.; Supasitmongkol, S.; Phongakorn, M. Combined Steam and CO₂ Reforming of Methane over the Hierarchical Ni–ZrO₂ Nanosheets/Al₂O₃ Catalysts at Ultralow Temperature and under Low Steam. *ACS Omega* **2023**, *8*, 46425–46437. [\[CrossRef\]](#)
- Ratana, T.; Jadsadajerm, S.; Tungkamani, S.; Sumarasingha, W.; Phongakorn, M. Effect of modified surface of Co/Al₂O₃ on properties and catalytic performance for CO₂ reforming of methane. *J. Phys. Chem. Solids* **2024**, *191*, 112034. [\[CrossRef\]](#)
- Diez, D.; Urueña, A.; Antolín, G. Investigation of Ni–Fe–Cu-layered double hydroxide catalysts in steam reforming of toluene as a model compound of biomass tar. *Processes* **2020**, *9*, 76. [\[CrossRef\]](#)
- Matusik, J. Layered double hydroxides (LDH) and LDH-based hybrid composites. *Materials* **2021**, *14*, 2582. [\[CrossRef\]](#)
- Michalik, A.; Napruszewska, B.D.; Walczyk, A.; Kryściak-Czerwenka, J.; Duraczyńska, D.; Serwicka, E.M. Synthesis of nanocrystalline Mg–Al hydrotalcites in the presence of starch—The effect on structure and composition. *Materials* **2020**, *13*, 602. [\[CrossRef\]](#) [\[PubMed\]](#)
- Amin, M.H. Relationship between the pore structure of mesoporous silica supports and the activity of nickel nanocatalysts in the CO₂ reforming of methane. *Catalysts* **2020**, *10*, 51. [\[CrossRef\]](#)

26. Li, M.; Cheng, J.P.; Wang, J.; Liu, F.; Zhang, X.B. The growth of nickel-manganese and cobalt-manganese layered double hydroxides on reduced graphene oxide for supercapacitor. *Electrochim. Acta* **2016**, *206*, 108–115. [\[CrossRef\]](#)
27. Debek, R.; Zubek, K.; Motak, M.; Galvez, M.E.; Da Costa, P.; Grzybek, T. Ni-Al hydrotalcite-like material as the catalyst precursors for the dry reforming of methane at low temperature. *Comptes Rendus Chim.* **2015**, *18*, 1205–1210. [\[CrossRef\]](#)
28. Wang, Z.; Jiang, X.; Pan, M.; Shi, Y. Nano-scale pore structure and its multi-fractal characteristics of tight sandstone by N₂ adsorption/desorption analyses: A case study of shihezi formation from the sulige gas field, ordos basin, china. *Minerals* **2020**, *10*, 377. [\[CrossRef\]](#)
29. Das, S.; Sengupta, M.; Patel, J.; Bordoloi, A. A study of the synergy between support surface properties and catalyst deactivation for CO₂ reforming over supported Ni nanoparticles. *Appl. Catal. A Gen.* **2017**, *545*, 113–126. [\[CrossRef\]](#)
30. Farooqi, A.S.; Yusuf, M.; Zabidi, N.A.M.; Saidur, R.; Sanaullah, K.; Farooqi, A.S.; Abdullah, B. A comprehensive review on improving the production of rich-hydrogen via combined steam and CO₂ reforming of methane over Ni-based catalysts. *Int. J. Hydrogen Energy* **2021**, *46*, 31024–31040. [\[CrossRef\]](#)
31. Abd Ghani, N.A.; Azapour, A.; Syed Muhammad, S.A.F.; Mohamed Ramli, N.; Vo, D.V.N.; Abdullah, B. Dry reforming of methane for syngas production over Ni–Co–supported Al₂O₃–MgO catalysts. *Appl. Petrochem. Res* **2018**, *8*, 263–270. [\[CrossRef\]](#)
32. Ha, Q.L.M.; Armbruster, U.; Atia, H.; Schneider, M.; Lund, H.; Agostini, G.; Martin, A. Development of active and stable low nickel content catalysts for dry reforming of methane. *Catalysts* **2017**, *7*, 157. [\[CrossRef\]](#)
33. High, M.; Patzschke, C.F.; Zheng, L.; Zeng, D.; Gavalda-Diaz, O.; Ding, N.; Song, Q. Precursor engineering of hydrotalcite-derived redox sorbents for reversible and stable thermochemical oxygen storage. *Nat. Commun.* **2022**, *13*, 5109. [\[CrossRef\]](#) [\[PubMed\]](#)
34. Debek, R.; Motak, M.; Galvez, M.E.; Grzybek, T.; Da Costa, P. Promotion effect of zirconia on Mg(Ni,Al)O mixed oxides derived from hydrotalcites in CO₂ methane reforming. *Appl. Catal. B Environ.* **2018**, *223*, 36–46. [\[CrossRef\]](#)
35. Wang, F.; Yang, X.; Zhang, J. Well-dispersed MgAl₂O₄ supported Ni catalyst with enhanced catalytic performance and the reason of its deactivation for long-term dry methanation reaction. *Catalysts* **2021**, *11*, 1117. [\[CrossRef\]](#)
36. Kannan, P.; Maiyalagan, T.; Marsili, E.; Ghosh, S.; Niedziolka-Jönsson, J.; Jönsson-Niedziolka, M. Hierarchical 3-dimensional nickel-iron nanosheet arrays on carbon fiber paper as a novel electrode for non-enzymatic glucose sensing. *Nanoscale* **2016**, *8*, 843–855. [\[CrossRef\]](#)
37. Shin, S.A.; Alizadeh Eslami, A.; Noh, Y.S.; Song, H.T.; Kim, H.D.; Ghaffari Saeidabad, N.; Moon, D.J. Preparation and Characterization of Ni/ZrTiAlO_x Catalyst via Sol-Gel and Impregnation Methods for Low Temperature Dry Reforming of Methane. *Catalysts* **2020**, *10*, 1335. [\[CrossRef\]](#)
38. Al-Doghachi, F.A.J.; Islam, A.; Zainal, Z.; Saiman, M.I.; Embong, Z.; Taufiq-Yap, Y.H. High coke-resistance Pt/Mg_{1-x}Ni_xO catalyst for dry reforming of methane. *PLoS ONE* **2016**, *11*, e0145862. [\[CrossRef\]](#) [\[PubMed\]](#)
39. Mastuli, M.S.; Kasim, M.F.; Mahat, A.M.; Asikin-Mijan, N.; Sivasangar, S.; Taufiq-Yap, Y.H. Structural and catalytic studies of Mg_{1-x}Ni_xO nanomaterials for gasification of biomass in supercritical water for H₂-rich syngas production. *Int. J. Hydrogen Energy* **2020**, *45*, 33218–33234. [\[CrossRef\]](#)
40. Siang, T.J.; Pham, T.L.; Van Cuong, N.; Phuong, P.T.; Phuc, N.H.H.; Truong, Q.D.; Vo, D.V.N. Combined steam and CO₂ reforming of methane for syngas production over carbon-resistant boron-promoted Ni/SBA-15 catalysts. *Microporous Mesoporous Mater.* **2018**, *262*, 122–132. [\[CrossRef\]](#)
41. Millet, M.M.; Tarasov, A.V.; Girgsdies, F.; Algara-Siller, G.; Schlögl, R.; Frei, E. Highly Dispersed Ni⁰/Ni_xMg_{1-x}O Catalysts Derived from Solid Solutions: How Metal and Support Control the CO₂ Hydrogenation. *ACS Catal.* **2019**, *9*, 8534–8546. [\[CrossRef\]](#)
42. Karuppiah, J.; Reddy, E.L.; Mok, Y.S. Anodized aluminum oxide supported NiO–CeO₂ catalyst for dry reforming of propane. *Catalysts* **2016**, *6*, 154. [\[CrossRef\]](#)
43. Loc, L.C.; Phuong, P.H.; Tri, N. Role of CeO₂ promoter in NiO/α-Al₂O₃ catalyst for dry reforming of methane. *Proceeding Name AIP Conf.* **2017**, *1878*, 020033.
44. Cárdenas-Arenas, A.; Bailón-García, E.; Lozano-Castelló, D.; Da Costa, P.; Bueno-López, A. Stable NiO–CeO₂ nanoparticles with improved carbon resistance for methane dry reforming. *J. Rare Earths* **2022**, *40*, 57–62. [\[CrossRef\]](#)
45. Yahi, N.; Menad, S.; Rodríguez-Ramos, I. Dry reforming of methane over Ni/CeO₂ catalysts prepared by three different methods. *Green Process. Synth.* **2015**, *4*, 479–486. [\[CrossRef\]](#)
46. Rui, N.; Zhang, X.; Zhang, F.; Liu, Z.; Cao, X.; Xie, Z.; Liu, C.J. Highly active Ni/CeO₂ catalyst for CO₂ methanation: Preparation and characterization. *Appl. Catal. B Environ.* **2021**, *282*, 119581. [\[CrossRef\]](#)
47. Marinho, A.L.A.; Toniolo, F.S.; Noronha, F.B.; Epron, F.; Duprez, D.; Bion, N. Highly active and stable Ni dispersed on mesoporous CeO₂–Al₂O₃ catalysts for production of syngas by dry reforming of methane. *Appl. Catal. B Environ.* **2021**, *281*, 119459. [\[CrossRef\]](#)
48. Singha, R.K.; Shukla, A.; Yadav, A.; Adak, S.; Iqbal, Z.; Siddiqui, N.; Bal, R. Energy efficient methane tri-reforming for synthesis gas production over highly coke resistant nanocrystalline Ni–ZrO₂ catalyst. *Appl. Energy* **2016**, *178*, 110–125. [\[CrossRef\]](#)
49. Greluk, M.; Rotko, M.; Słowik, G.; Turczyniak-Surdacka, S.; Grzybek, G.; Góra-Marek, K.; Kotarba, A. Effect of potassium promoter on the performance of cobalt catalysts on steam reforming of ethanol. *Catalysts* **2022**, *11*, 600. [\[CrossRef\]](#)
50. Okhlopkova, L.; Prosvirin, I.; Kerzhentsev, M.; Ismagilov, Z. Combined Steam and CO₂ Reforming of Methane over Ni-Based CeO₂–MgO Catalysts: Impacts of Preparation Mode and Pd Addition. *Appl. Sci.* **2023**, *13*, 4689. [\[CrossRef\]](#)
51. Vacharapong, P.; Arayawate, S.; Katanyutanon, S.; Toochinda, P.; Lawtrakul, L.; Charojrochkul, S. Enhancement of Ni catalyst using CeO₂–Al₂O₃ support prepared with magnetic inducement for ESR. *Catalysts* **2020**, *10*, 1357. [\[CrossRef\]](#)

52. Tapia-P, J.; Gallego, J.; Espinal, J.F. Calcination Temperature Effect in Catalyst Reactivity for the CO SELOX Reaction Using Perovskite-like LaBO_3 (B: Mn, Fe, Co, Ni) Oxides. *Catal. Lett.* **2021**, *151*, 3690–3703. [\[CrossRef\]](#)
53. Zeng, Q.; Xie, W.; Chen, Z.; Wang, X.; Akinoglu, E.M.; Zhou, G.; Shui, L. Influence of the facets of $\text{Bi}_{24}\text{O}_{31}\text{Br}_{10}$ nanobelts and nanosheets on their photocatalytic properties. *Catalysts* **2020**, *10*, 257. [\[CrossRef\]](#)
54. Li, M.; Wang, X.; Cárdenas-Lizana, F.; Keane, M.A. Effect of support redox character on catalytic performance in the gas phase hydrogenation of benzaldehyde and nitrobenzene over supported gold. *Catal. Today* **2017**, *279*, 19–28. [\[CrossRef\]](#)
55. Ebiad, M.A.; Abd El-Hafiz, D.R.; Elsalamony, R.A.; Mohamed, L.S. Ni supported high surface area $\text{CeO}_2\text{-ZrO}_2$ catalysts for hydrogen production from ethanol steam reforming. *RSC Adv.* **2012**, *2*, 8145–8156. [\[CrossRef\]](#)
56. Li, L.; Wang, Y.; Zhao, Q.; Hu, C. The effect of Si on CO_2 methanation over Ni-xSi/ZrO catalysts at low temperature. *Catalysts* **2021**, *11*, 67. [\[CrossRef\]](#)
57. Sikander, U.; Sufian, S.; Salam, M.A. A review of hydrotalcite based catalysts for hydrogen production systems. *Int. J. Hydrogen Energy* **2017**, *42*, 19851–19868. [\[CrossRef\]](#)
58. Phuong, P.H.; Loc, L.C.; Tri, N.; Anh, N.P.; Anh, H.C. Effect of NH_3 Alkalization and MgO Promotion on the Performance of Ni/SBA-15 Catalyst in Combined Steam and Carbon Dioxide Reforming of Methane. *J. Nanomater.* **2021**, *2021*, 5570866. [\[CrossRef\]](#)
59. Dan, M.; Mihet, M.; Borodi, G.; Lazar, M.D. Combined steam and dry reforming of methane for syngas production from biogas using bimodal pore catalysts. *Catal. Today* **2020**, *366*, 87–96.
60. Radlik, M.; Adamowska-Teyssier, M.; Krztoń, A.; Koziół, K.; Krajewski, W.; Turek, W.; Da Costa, P. Dry reforming of methane over Ni/ $\text{Ce}_{0.62}\text{Zr}_{0.38}\text{O}_2$ catalysts: Effect of Ni loading on the catalytic activity and on H_2/CO production. *Comptes Rendus Chim.* **2015**, *8*, 1242–1249. [\[CrossRef\]](#)
61. Huang, H.; Zhang, X.; Liu, J.; Ye, S. Study on oxidation activity of Ce–Mn–K composite oxides on diesel soot. *Sci. Rep.* **2020**, *10*, 10025. [\[CrossRef\]](#)
62. Wang, K.; Liu, X.; Tu, S.; Zhang, L.; Jiang, C.; Li, W.; Ye, D. Catalytic Oxidation of Toluene over Manganese and Cerium Complex Oxide Supported on Zeolite. *J. Phys. Conf. Ser.* **2020**, *1676*, 012064. [\[CrossRef\]](#)
63. Weng, X.; Shi, B.; Liu, A.; Sun, J.; Xiong, Y.; Wan, H.; Chen, Y.W. Highly dispersed Pd/modified- Al_2O_3 catalyst on complete oxidation of toluene: Role of basic sites and mechanism insight. *Appl. Surf. Sci.* **2019**, *497*, 143747. [\[CrossRef\]](#)
64. Siang, T.J.; Danh, H.T.; Singh, S.; Truong, Q.D.; Setiabudi, H.D.; Vo, D.V.N. Syngas production from combined steam and carbon dioxide reforming of methane over Ce-modified silica supported nickel catalysts. *Chem. Eng. Trans.* **2017**, *56*, 1129–1134.
65. Sangsong, S.; Ratana, T.; Tungkamani, S.; Sornchamni, T.; Phongaksorn, M. Effect of CeO_2 loading of the Ce–Al mixed oxide on ultrahigh temperature water-gas shift performance over Ce–Al mixed oxide supported Ni catalysts. *Fuel* **2019**, *252*, 488–495. [\[CrossRef\]](#)
66. Koo, K.Y.; Lee, S.H.; Jung, U.H.; Roh, H.S.; Yoon, W.L. Syngas production via combined steam and carbon dioxide reforming of methane over Ni–Ce/ MgAl_2O_4 catalysts with enhanced coke resistance. *Fuel Process. Technol.* **2014**, *119*, 151–157. [\[CrossRef\]](#)
67. Abdulrasheed, A.; Jalil, A.A.; Gambo, Y.; Ibrahim, M.; Hambali, H.U.; Shahul Hamid, M.Y. A review on catalyst development for dry reforming of methane to syngas: Recent advances. *Renew. Sustain. Energy Rev.* **2019**, *108*, 175–193. [\[CrossRef\]](#)
68. Zhao, Z.; Ren, P.; Li, W.; Miao, B. Effect of mineralizers for preparing ZrO_2 support on the supported Ni catalyst for steam- CO_2 bi-reforming of methane. *Int. J. Hydrogen Energy* **2017**, *42*, 6598–6609. [\[CrossRef\]](#)
69. Chen, L.; Qi, Z.; Zhang, S.; Su, J.; Somorjai, G.A. Catalytic hydrogen production from methane: A review on recent progress and prospect. *Catalysts* **2020**, *10*, 858. [\[CrossRef\]](#)
70. Nabgan, W.; Nabgan, B.; Abdullah, T.A.T.; Ngadi, N.; Jalil, A.A.; Hassan, N.S.; Majeed, F.S.A. Conversion of polyethylene terephthalate plastic waste and phenol steam reforming to hydrogen and valuable liquid fuel: Synthesis effect of Ni–Co/ ZrO_2 nanostructured catalysts. *Int. J. Hydrogen Energy* **2020**, *45*, 6302–6317. [\[CrossRef\]](#)
71. Bang, S.; Hong, E.; Baek, S.W.; Shin, C.H. Effect of acidity on Ni catalysts supported on P-modified Al_2O_3 for dry reforming of methane. *Catal. Today* **2018**, *303*, 100–105. [\[CrossRef\]](#)

Disclaimer/Publisher’s Note: The statements, opinions and data contained in all publications are solely those of the individual author(s) and contributor(s) and not of MDPI and/or the editor(s). MDPI and/or the editor(s) disclaim responsibility for any injury to people or property resulting from any ideas, methods, instructions or products referred to in the content.